water

MDPI

Article

Synthesis of Sulfur-Doped Magnetic Iron Oxides for Efficient Removal of Lead from Aqueous Solutions

Junqing Xu [1,†], Meitian Pan [1,†], Cong Zou [2], Xueqiong Huang [2], Takeshi Hagio [3], Ryoichi Ichino [3], Long Kong [2,*] and Liang Li [2,*]

1 China-UK Low Carbon College, Shanghai Jiao Tong University, Shanghai 201306, China
2 School of Environment Science and Engineering, Shanghai Jiao Tong University, Shanghai 200240, China
3 Institutes of Innovation for Future Society, Nagoya University, Nagoya 464-8603, Japan; hagio@mirai.nagoya-u.ac.jp (T.H.); ichino@numse.nagoya-u.ac.jp (R.I.)
* Correspondence: longmao88@sjtu.edu.com (L.K.); liangli117@sjtu.edu.cn (L.L.); Tel.: +86-5474-7567 (L.K. & L.L.)
† These authors contributed equally to this work.

Abstract: Heavy metal pollution poses an environmental risk, and its efficient removal and facile separation from water remains a challenge. Magnetic iron oxide, an eco-friendly, relatively stable, and easy-separation material, has been regarded as one of the most applicable adsorbents for water treatment. However, the limited adsorption capacity has restricted its applications. Herein, sulfur-doped magnetic Fe_3O_4 (S_x–Fe_3O_4) adsorbent was fabricated using a calcination method for the efficient removal of Pb(II) from water. In contrast to undoped Fe_3O_4, the introduction of doped sulfur greatly enhanced the adsorption performance of S–Fe_3O_4 over four times, with a maximum capacity of 333.33 mg g^{-1}, which was synthesized at 300 °C with a raw molar ratio of S–Fe of 5. Based on the structure and morphology analysis, it was demonstrated that sulfur was successfully doped into the Fe_3O_4 structures, which resulted in Fe_3O_4 with active sulfur sites accordingly contributing to the adsorption enhancement through the combination of strong soft–soft interactions between soft base sulfur and soft acid Pb(II) along with surface adsorption. S_x–Fe_3O_4 could maintain the adsorption performance in the presence of competing ions. Furthermore, although the sulfur doping process exhibited slight side effects on the magnetic property, magnetic S_x–Fe_3O_4 maintained the high separation potential. This study presented a promising strategy to enhance the adsorption performance of Fe_3O_4 through sulfur doping for Pb(II) removal from water.

Keywords: adsorption; Pb; sulfur-doped Fe_3O_4; water treatment

check for updates

Citation: Xu, J.; Pan, M.; Zou, C.; Huang, X.; Hagio, T.; Ichino, R.; Kong, L.; Li, L. Synthesis of Sulfur-Doped Magnetic Iron Oxides for Efficient Removal of Lead from Aqueous Solutions. *Water* **2023**, *15*, 3667. https://doi.org/10.3390/w15203667

Academic Editors: Xin Zhou, Meimei Zhou and Jing Yang

Received: 3 September 2023
Revised: 3 October 2023
Accepted: 4 October 2023
Published: 20 October 2023

1. Introduction

Heavy metal pollution poses a serious threat to human health and the eco–environment due to its characteristics of high toxicity, nondegradation, and easy bioaccumulation [1–3]. The water pollution from heavy metals has become a global environmental issue with the rapid development of industry [3]. The development of industries such as mining, lead batteries, paints, refining, and so on has led to heavy metal water pollution through waste effluents. Approximately 40% of lakes and rivers on Earth are polluted with heavy metals [4]. Rivers, wetlands, and bays in the United States, Japan, India, and China all occurred the pollution of heavy metals. Accordingly, both the WHO and China have established maximum allowable limits for these toxic heavy metals in drinking water. Therefore, the strategy for treating heavy-metal-polluted water has attracted widespread attention to remove heavy metals from contaminated water. In recent years, various strategies, including chemical precipitation [5], membrane [1], ion exchange, and adsorption, have been developed to remove heavy metals from water. Among them, although precipitation is a simple and widely applied process, it usually is not effective for reducing the heavy metal concentration to a low level. And the application of a membrane system meets

major issues like membrane fouling and blocking, while the ion exchange strategy requires the utilization of high-cost resin. Adsorption, as an economically feasible, efficient, and easy-to-operate strategy, has been widely developed and put into practical application [1,6]. The performance of the adsorption system is reliant on the characteristics of the adsorbent to a large extent. Exploring adsorbents that combine high adsorption capacity, superior affinity, and easy separation is vital but also faces challenges.

Various types of materials have been extensively studied for the removal of heavy metals from water [1,6–9]. Among them, magnetic iron oxides, as eco-friendly, relatively stable, and easy-separation materials, have been regarded as one of the most applicable adsorbents for water treatment [10–13]. However, the heavy metal removal capability of iron oxides is not satisfied, especially under the large amounts of coexisting ions in wastewater. Therefore, in recent years, extensive efforts have been made for the development of magnetic nano Fe_3O_4 and their surface modification, including thiol groups [14,15], amine groups [16], carboxylate ligands [17], or polymer [18] to achieve the desired effectiveness in the heavy metal removal, taking advantage of its adsorption performance and facile magnetic separation.

To endow the nano Fe_3O_4 with superior adsorption, much attention has been paid to the thiol groups since they showed a strong affinity toward heavy metal ions due to the soft base of sulfur and soft acid of heavy metals like Hg^{2+} [14], Pb^{2+} [15], and Cd^{2+} [14,19], thereby enhancing the adsorption selectivity and performance. Accordingly, sulfur plays a vital role in the removal of Hg^{2+}, Pb^{2+}, and Cd^{2+}. Considering the vital role of sulfur for heavy metal adsorption, in addition to the thiol organic ligands, there is also an increasing amount of research on the development of inorganic sulfur-containing materials. As previously reported, it is generally recognized that the eco-friendly iron sulfides as an iron-based adsorbent exhibit a strong capability for selectively removing heavy metal cations from aqueous solution because of being inherently rich in sulfur [20–22]. However, the stability issue of iron sulfides imposes limitations on their application, which may experience passivation in water when exposed to air [23], leading to utilization constantly proceeding under the protection of an inert atmosphere [22,24]. In addition, the difficult separation issue of iron sulfides also poses limitations on their application. Given the attractive features of Fe_3O_4 and iron sulfides, if we combine their advantages together, i.e., the stability of Fe_3O_4 and the heavy metal affinity of sulfides, it could be a potential material to achieve effective removal and magnetic separation of heavy metals from water. Actually, besides the modification of organic ligands, the element doping approach, usually multivalent metal cationic, has been generally believed to enhance the adsorption performance of iron oxides in a previous report [25–27]. Sulfur may be a favored doping component to improve the heavy metal adsorption capacity due to its high affinity toward Lewis acid heavy metal cations. Inspired by this concept, we aim to introduce sulfur to Fe_3O_4 nanoparticles through a doping strategy to achieve an effective magnetic adsorbent. To the best of our knowledge, there are rare studies that have reported on the sulfur-doped Fe_3O_4 (S_x–Fe_3O_4) for the removal of heavy metals. The sulfur-doped magnetic Fe_3O_4 adsorbents guaranteed the removal capacity of Pb(II) and the facile separation of adsorbent from water.

In this study, S_x–Fe_3O_4 was constructed via a facile calcination method to successfully dope sulfur into Fe_3O_4 nanoparticles. A series of S_x–Fe_3O_4 was synthesized by changing the calcination temperature and the ratio of doped sulfur ratio; accordingly, the effects of calcination temperature and sulfur content on the adsorption capability of Pb(II) were examined. The crystal structure, morphology, surface structure, and magnetic properties of S–Fe_3O_4 were analyzed through XRD, TEM, FTIR, and VSM. Here, Pb(II) was selected to evaluate the heavy metal adsorption performance of S_x–Fe_3O_4. Comprehensive adsorption experiments were carried out to determine the adsorption kinetic capacity of Pb(II) with S_x–Fe_3O_4 compared to Fe_3O_4. The coexisting cations experiment was also carried out to investigate the selectivity for Pb(II). This work demonstrated the potential of the sulfur doping approach for developing effective magnetic adsorbents to selectively remove and separate Pb(II) from water.

2. Materials and Methods

2.1. Chemicals

$Fe(NO_3)_3 \cdot 9H_2O$, thioacetamide (>99%), and butylamine were provided by Aladdin Chemical (Shanghai, China). Methanol, acetone, calcium chloride, magnesium chloride, zinc chloride, cadmium chloride, and copper chloride were all provided by Sinopharm Chemical Reagent Co., Ltd. (Shanghai, China). All chemicals were utilized without any further purification in the work. Distilled water (>18 MΩcm) was used in the preparation of Pb(II) solution.

2.2. Preparation of S_x–Fe_3O_4

Preparation of sulfur-doped magnetite nanoparticles involves the following steps: $Fe(NO_3)_3 \cdot 9H_2O$ and thiourea are separately dispersed in n-butylamine using ultrasonication (total volume of 50 mL). The two solutions are then mixed in a three-necked flask with a capacity of 250 mL. The reaction is carried out under continuous magnetic stirring in a flowing inert gas environment, at a temperature of 60 °C for 2 h. After natural cooling to room temperature, the supernatant is removed using high-speed centrifugation. The solid material is washed several times with methanol and acetone, followed by vacuum drying at 60 °C for 1 h to obtain the precursor material. The precursor material is placed in a muffle furnace and calcined at a set temperature for 2 h, with a continuous inflow of inert gas. After sufficient cooling, the resulting nanomaterial is thoroughly ground, yielding S_x–Fe_3O_4 nanoparticles. To make a comparison, Fe_3O_4 nanoparticles without sulfur doping are prepared using the same steps (except for the absence of thiourea). The molar ratio of $Fe(NO_3)_3 \cdot 9H_2O$ to thiourea is adjusted to 1:0.5, 1:1, 1:2, 1:3, 1:4, and 1:5, while the ratio of $Fe(NO_3)_3 \cdot 9H_2O$ to n-butylamine is 1 mmol:10 mL. The samples prepared under different raw material ratios are labeled as $S_{0.5}$–Fe_3O_4, S_1–Fe_3O_4, S_2–Fe_3O_4, S_3–Fe_3O_4, S_4–Fe_3O_4, and S_5–Fe_3O_4. The high-temperature calcination is performed at temperatures of 200 °C, 250 °C, 300 °C, 400 °C, and 500 °C, and the molar ratio of raw sulfur to iron is 5. The resulting samples are labeled as S–Fe_3O_4-200, S–Fe_3O_4-250, S–Fe_3O_4-300, S–Fe_3O_4-400, and S–Fe_3O_4-500, respectively.

2.3. Characteristics of S–Fe_3O_4

X-ray Diffraction (XRD): XRD measurements were performed using a Shimadzu XRD-6100 X-ray diffractometer with Cu Kα radiation (Shimadzu Corporation, Kyoto, Japan). The X-ray tube operated at 40 kV, and the scanning range (2θ) was set from 10° to 90° with a scanning speed of 10°/min. Transmission Electron Microscopy (TEM): TEM analysis was conducted using a JEOL JEM-2100F transmission electron microscope from JEOL Ltd., Akishima, Japan. X-ray Photoelectron Spectroscopy (XPS): XPS analysis was carried out using a Thermo Scientific Escalab 250Xi X-ray photoelectron spectrometer from Thermo Fisher Scientific, Waltham, MA, USA. Al Kα monochromatic radiation was used as the X-ray source. Fourier Transform Infrared Spectroscopy (FTIR): FTIR analysis was performed using a Thermo Nicolet 6700 spectrometer (Thermo Fisher Scientific, Waltham, MA, USA). The spectra were recorded in the range of 4000–400 cm^{-1} using KBr as the reference material. Vibrating Sample Magnetometer (VSM): VSM measurements were conducted using an MG L-1S-9T (EC-II) VSM instrument from Quantum Design, San Diego, CA, USA. The magnetic field range was −3 T to 3 T, and the temperature control range was from 1.9 K to 300 K with a temperature control accuracy of ±1% (from zero field to −9 T). Energy Dispersive X-ray Fluorescence Spectroscopy (ED-XRF): ED-XRF analysis was performed using an EDX-700 instrument from Shimadzu Corporation, Kyoto, Japan.

2.4. Adsorption of Lead from Water

The adsorption of Pb(II) by the prepared material was conducted under constant-temperature agitation. In the kinetic study, 60 mg of the adsorbent was added to 100 mL of Pb(II) solution (100 mg L^{-1}) while maintaining continuous stirring for 24 h. At stetted time intervals, aliquots of the aqueous solution were withdrawn and filtered through a

0.22 μm membrane. Adsorption isotherm experiments were conducted in 50 mL of Pb(II) solution with concentrations ranging from 5 to 500 mg L^{-1}, with 25 mg of adsorbent added separately. The bottles were shaken for 24 h to approach adsorption equilibrium. To assess the impact of their competing, calcium chloride, magnesium chloride, zinc chloride, cadmium chloride, and copper chloride were individually added to the lead solution (100 mg L^{-1}). The concentrations of competing ions were set as 0.50 and 1.00 mmol to investigate their influence on Pb(II) removal, respectively. The Pb(II) concentrations in the filtrates were analyzed using an atomic adsorption spectrometer (Analytik Jena AG, ControlAA700, Jena, Germany).

3. Results and Discussion

3.1. The Morphology and Structure of S–Fe_3O_4

Sulfur-doped Fe_3O_4 adsorbents were synthesized under different calcination temperatures and sulfur contents. The XRD patterns of Fe_3O_4 and S_x–Fe_3O_4 are shown in Figure 1. It can be seen that the crystal structure of iron oxide changes with the synthesiz temperature. Under low-temperature conditions (200 °C), it is mostly poorly crystalline, with broad peaks approximately at 35°, indicating incomplete formation of the Fe_3O_4 crystalline phase. With the rise in synthesizing temperature, the XRD peaks corresponding to Fe_3O_4 become stronger; this suggests the increase in crystallinity. This means that higher calcination temperatures facilitate the crystallization of Fe_3O_4. Thus, a well-defined crystalline structure of Fe_3O_4 nanoparticles can form through calcination at 300 °C and 400 °C. Distinct diffraction peaks are indexed to the characteristic diffraction peaks of the (220), (311), (400), (511), and (440) planes of magnetite Fe_3O_4 (JCPDS 19-0629), indicating the formation of a well-crystallized Fe_3O_4 structure. However, a phase transition of the iron oxide to Fe_2O_3 (JCPDS 33-0664) occurs when the temperature rises to 500 °C. Afterwards, S_x–Fe_3O_4 adsorbents doping with different sulfur contents are prepared at 300 °C to determine the influence of sulfur doping on their crystalline structure. It is noteworthy that the doping of sulfur causes a slight shift of characteristic peaks towards smaller angles compared to the undoped Fe_3O_4, as shown in Figure 1b. Additionally, the magnitude of the shift towards smaller angles increases with the increasing doping level of sulfur. This could be attributed to the incorporation of sulfur with larger atoms into the Fe_3O_4 [28] and also demonstrated the successful synthesizing of S_x–Fe_3O_4. Overall, the structure from XRD indicates that the sulfur has been successfully doped in the well-crystallized Fe_3O_4, which would contribute to the higher adsorption capacity toward heavy metals.

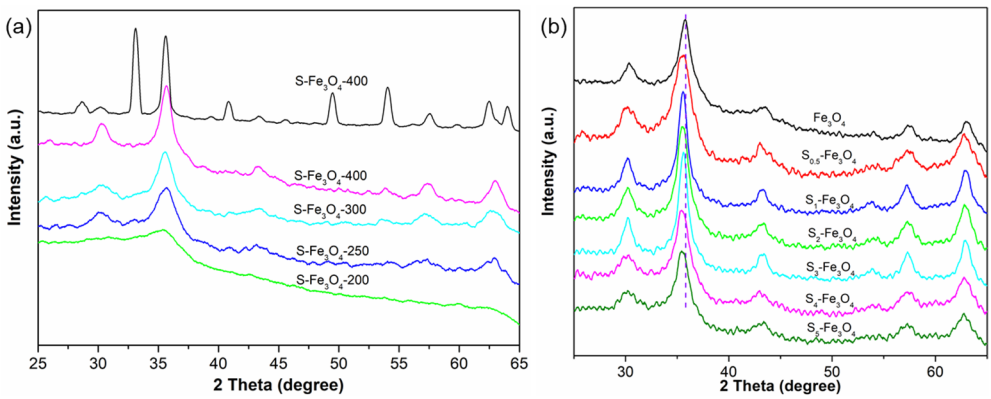

Figure 1. XRD patterns of the S_x–Fe_3O_4 NPs and Fe_3O_4 NPs (**a**) prepared under different temperatures and (**b**) with different S: Fe molar ratios.

The morphologies of S_x–Fe_3O_4 nanoparticles synthesized at different calcination temperatures and Fe_3O_4 were investigated, as illustrated in Figure 2. It can be observed that S–Fe_3O_4-200 exhibited mostly an amorphous structure and has not yet formed a well-defined nanoparticle structure, which is consistent with the XRD results. On the contrary, with the rise in the calcination temperature, the morphologies of S_x–Fe_3O_4 be-

came more regular with well-defined nanoparticle structures and crystalline arrangements. This means that a certain synthesizing temperature is needed to drive the formation of crystalline S–Fe_3O_4. Additionally, clear lattice fringes can be observed in their HR-TEM images, indicating the good crystallinity of the nanoparticles. The average particle sizes of S–Fe_3O_4-250, S–Fe_3O_4-300, S–Fe_3O_4-400, and S–Fe_3O_4-500 are 8.99 nm, 10.52 nm, 11.17 nm, and 14.04 nm, respectively. Without sulfur doping, Fe_3O_4-300 exhibited a larger average particle size in comparison with S–Fe_3O_4-300 synthesized at the same temperature. It can be observed that temperature has a certain influence on the nanoparticle size, with higher temperatures leading to larger S_x–Fe_3O_4 particle sizes. TEM characterization further confirms that even after the introduction of sulfur, Fe_3O_4 maintains its particle and well-defined crystalline structure.

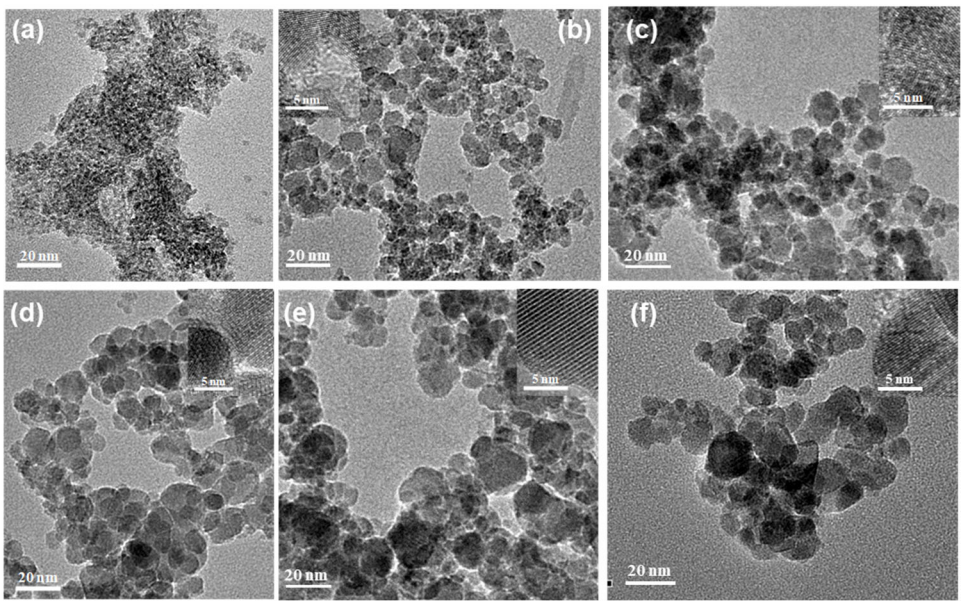

Figure 2. TEM images of the prepared S_x–Fe_3O_4 NPs synthesized at different temperatures and Fe_3O_4 NPs nanoparticles synthesized at 300 °C. (**a**) S–Fe_3O_4-200, (**b**) S–Fe_3O_4-250, (**c**) S–Fe_3O_4-300, (**d**) S–Fe_3O_4-400, (**e**) S–Fe_3O_4-500, and (**f**) Fe_3O_4-300.

The FTIR spectra of S_x–Fe_3O_4 synthesized at different temperatures and undoped Fe_3O_4 nanoparticles are shown in Figure 3a. The spectra of S_x–Fe_3O_4 synthesized at different temperatures all exhibit a characteristic absorption peak around 570 cm^{-1} that is derived from the typical vibration of the Fe–O [29], indicating that all these samples maintain their structural properties of iron oxides. There is no obvious change in S_x–Fe_3O_4 in comparison with Fe_3O_4 under the same calcination temperature except for the bands at 1039 cm^{-1} and 1403 cm^{-1}. This may be introduced from the incomplete decompose of groups [30,31]. The differences between S_x–Fe_3O_4 synthesized at different temperatures may be attributed to the variations of precursors in the annealing process and lead to the changes in surface groups. These peaks showed a decrease in intensity along with the increasing calcination temperature.

The magnetic properties of S_x–Fe_3O_4 at different calcination temperatures are conducted to evaluate the magnetic properties, as shown in Figure 3b. Based on measurements conducted in a physical property measurement system at 300 K and 3 T, S_x–Fe_3O_4 exhibits paramagnetism without significant hysteresis, which is beneficial for its magnetic separation from aqueous solutions. The saturation magnetization values of S–Fe_3O_4-200, S–Fe_3O_4-250, S–Fe_3O_4-300, S–Fe_3O_4-400, and S–Fe_3O_4-500 are measured to be 6.78, 19.04, 32.97, 31.51, and 18.39 emu g^{-1}, respectively. As the calcination temperature increases from 200 °C to 300 °C, the crystallinity of S–Fe_3O_4 nanoparticles improves; this accordingly enhances the thermal fluctuations of magnetic particles [32], resulting in the increase in saturation magnetization under the applied magnetic field. However, when the calcination

temperature continues rising to 500 °C, the saturation magnetization decreases significantly, which is due to the high-temperature calcination causing a phase transition from Fe_3O_4 to Fe_2O_3. Compared with the nonmagnetic sorbents that relied on the centrifugation for separation, the magnetic properties of S–Fe_3O_4 under an external magnetic field (Figure 3b) enable a facile approach to separate the adsorbent from water.

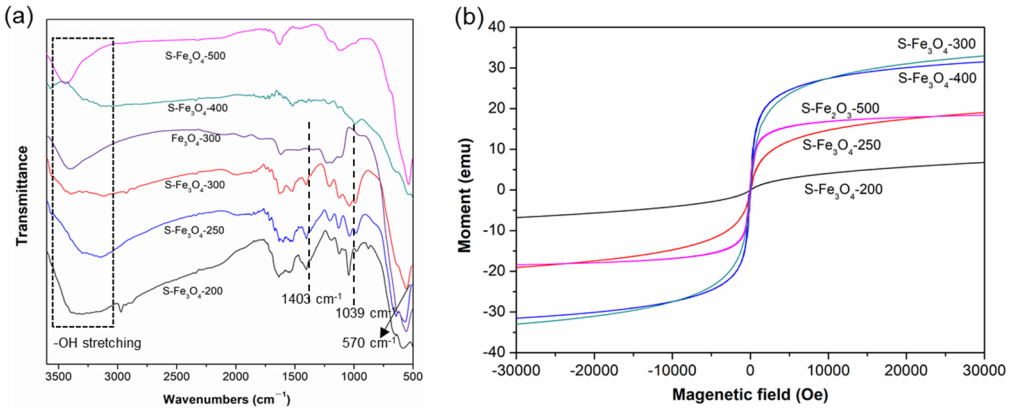

Figure 3. FTIR spectra (**a**) and magnetization curves (**b**) of S_x–Fe_3O_4 prepared under different temperatures.

3.2. Adsorption Performance of S_x–Fe_3O_4

The adsorption performances of S_x–Fe_3O_4 nanoparticles prepared under different calcination temperatures were evaluated. The variations of the adsorption capacity of Pb(II) with adsorption time were performed to determine the adsorption kinetics. As depicted in Figure 4a, S_x–Fe_3O_4 initially showed rapid adsorption and gradually reached equilibrium. The pseudo-first-order and pseudo-second-order kinetic models were applied to describe the Pb adsorption rates (Figures 4b and S1 and Table S1). The adsorption behavior can be well described by the pseudo-second-order model with higher correlation coefficients, suggesting that the adsorption behavior of Pb(II) with sulfur-doped Fe_3O_4 was essentially chemisorption and was controlled by the sorption process rather than diffusion [22].

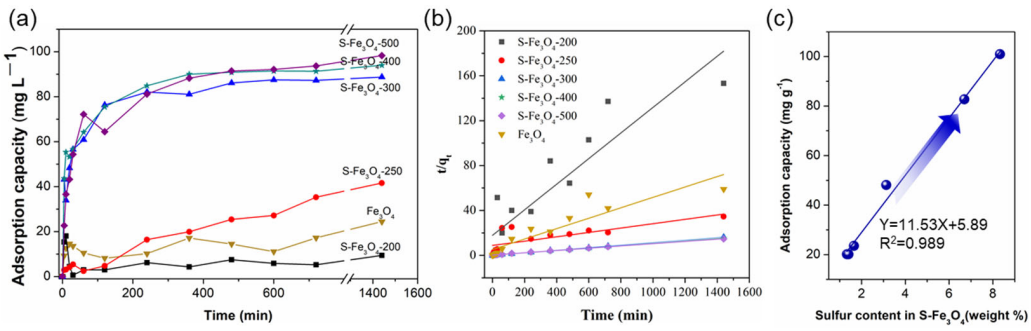

Figure 4. Adsorption kinetics (**a**) and the pseudo-second-order model fitting (**b**) of Pb(II) with S_x–Fe_3O_4 prepared at different temperatures. (**c**) Correlation between the doped sulfur content and adsorption capacity of Pb(II) (symbols are experimental data, solid lines represent the fitted curves).

In comparison with Fe_3O_4, the S_x–Fe_3O_4 presented a noticeable advantage, with higher adsorption rates and capacities except for the S–Fe_3O_4-200. Amorphous metal oxides are expected to show high adsorption performance in comparison with their crystalline phase [33,34]. Herein, S–Fe_3O_4-200 possessed a higher adsorption rate constant, suggesting the amorphous structure was beneficial for achieving a rapid adsorption process. However, the adsorption capacity of S–Fe_3O_4-200 was much lower than that of S_x–Fe_3O_4 synthesized at higher temperatures. As the calcination temperature increased, the adsorption capacity of magnetic S–Fe_3O_4-300 and S–Fe_3O_4-400 exhibited significant improvements of 90.91 mg g-1, which is over four times higher than that of Fe_3O_4. This can be attributed to

the higher temperatures that take a stable and crystalline structure, as well as the increased S content that provides strong and selective soft–soft interactions toward Pb(II) ions. However, as the synthesizing temperature continued to increase to 500 °C, the nonmagnetic S–Fe_3O_4-500 was formed with a slightly higher adsorption capacity. Overall, the obvious adsorption enhancement of S–Fe_3O_4 indicated the Pb(II) affinity mostly arising from the introduction of sulfur sites in Fe_3O_4. Taking into account the adsorption performance and separation, magnetic S–Fe_3O_4-300 and S–Fe_3O_4-400 hold superior adsorption kinetics and are readily recovered from aqueous solutions via a simple magnetic separation. These comparisons demonstrated the effects of calcination temperatures and sulfur content, and sulfur appeared to boost the active sites for Pb, thus making the S_x–Fe_3O_4 effective adsorbents.

In addition, to determine the influence of sulfur content on the adsorption capacity, we investigated the correlation between the Pb(II) adsorption behavior of S_x–Fe_3O_4 and the doped sulfur content using S–Fe_3O_4 with a different sulfur doping ratio. Within the investigated range, there is a linear correlation between the adsorption capacity and the accurate sulfur content in S_x–Fe_3O_4, basing the XRF data (Table S2) with a high R^2 0.989, as shown in Figure 4c. When the sulfur ratio continues increasing, overloaded doping ions may influence the structure of iron oxides, resulting in a less stable adsorption process with fluctuations and a slight decline in adsorption capacity. As presented by the superior adsorption performance of S_x–Fe_3O_4, the doped sulfur plays a key role and facilitates the removal of Pb(II) because the sulfur doped in iron oxides is the active adsorption site of Pb, and more sulfur sites would contribute to the higher adsorption capacity through soft–soft interactions of Lewis acid Pb(II).

The adsorption isotherms of S_x–Fe_3O_4 for Pb(II) are investigated and shown in Figure 5. It can be observed that the adsorption capacities of adsorbents S_5–Fe_3O_4-300, S_5–Fe_3O_4-400 NPs, and S_4–Fe_3O_4-300 all increased gradually with increasing the initial Pb(II) concentration and reached their maximum capacities, respectively. Langmuir and Freundlich isotherm models were employed to fit the adsorption data. The fitting parameters obtained from the two adsorption isotherm models are summarized in Table 1. According to the correlation, the adsorption performance of S_x–Fe_3O_4 for Pb(II) could be well fitted by both the Freundlich and Langmuir models and better described by the Freundlich model, with higher correlation coefficients, especially for S_5–Fe_3O_4-300, indicating primarily a multilayered adsorption process. This might be caused by the asymmetrical adsorbent surface and different kinds of active sites [35]. The values of $1/n$ for all the prepared adsorbents of S_5–Fe_3O_4-300, S_5–Fe_3O_4-400, and S_4–Fe_3O_4-300 are between 0 and 1, indicating a favorable adsorption condition [36].

The theoretical maximum adsorption capacity of S_5–Fe_3O_4-300 is calculated to be 333.33 mg g^{-1}, which is two times higher than that of S_4–Fe_3O_4-300 (166.67 mg g^{-1}). This may result from the sulfur doping and appears to be dependent on the sulfur content in the adsorbent. And compared with the S_5–Fe_3O_4-400, S_5–Fe_3O_4-300 synthesized at a relatively lower temperature is favorable for enhancing the adsorption performance. S_5–Fe_3O_4-300 exhibited a facile adsorption performance of Pb(II). According to the influence of sulfur content on adsorption capacity, as shown in Figure 4c, the introduced sulfur played a key role in the removal of Pb(II) with S_x–Fe_3O_4. In addition, electrostatic attraction might be a point to influence the adsorption capacity. Pb(II) ions would undergo hydrolysis in an aqueous solution. A higher pH value favors the adsorption of Pb(II) to a large extent, and the specific surface area of the nano adsorbent provides abundant sites for positively charged Pb(II). Therefore, S_5–Fe_3O_4-300 carried more sulfur content with superior affinity toward Pb(II) and crystalline structure, which resulted in the highest adsorption capacity and most rapid adsorption kinetics and, therefore, was selected for further adsorption investigation. On the basis of the aforementioned analyses, it can be concluded that Pb (II) was removed from the aqueous solution through a combination of strong soft–soft interaction (Pb–S bond) and surface adsorption. These results demonstrated the potential of S_x–Fe_3O_4 as an effective sorbent for the decontamination of Pb(II) polluted water.

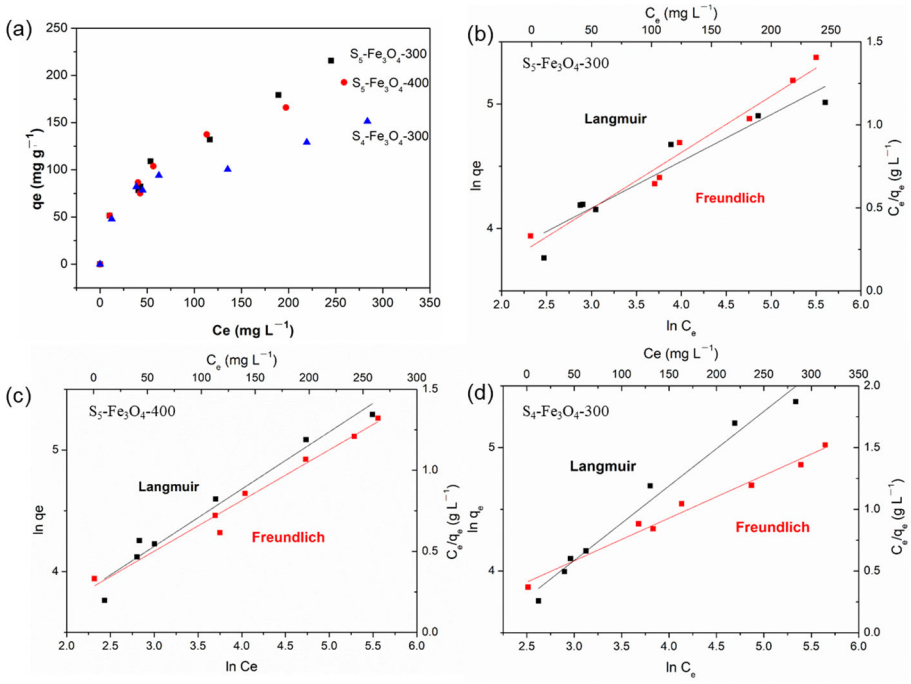

Figure 5. The adsorption isotherm (**a**) and fitting models of Pb(II) with S_5–Fe_3O_4-300 (**b**), S_5–Fe_3O_4-400 NPs (**c**), and S_4–Fe_3O_4-300 (**d**) (symbols are experimental data, solid lines represent the fitted curves).

Table 1. The fitting data calculated from Langmuir and Freundlich models for Pb(II) adsorption with S_x–Fe_3O_4.

Adsorbents	Langmuir			Freundlich		
	q_m	K_L	R^2	K_F	1/n	R^2
S_5–Fe_3O_4-300	333.33	0.0096	0.920	16.49	0.451	0.967
S_5–Fe_3O_4-400	250.00	0.0140	0.964	18.47	0.416	0.974
S_4–Fe_3O_4-300	166.67	0.0212	0.978	21.01	0.345	0.981

In general, the coexisting cations may compete with Pb(II) for the adsorption site. Considering the existence of ions in water, the influence of competing ions on the adsorption behavior of Pb(II) with S_x–Fe_3O_4 was investigated. Here, the Pb(II) adsorption performance of S_x–Fe_3O_4 was evaluated in the presence of Mg^{2+}, Ca^{2+}, Cd^{2+}, Cu^{2+}, and Zn^{2+}. As illustrated in Figure 6, the adsorption capabilities of prepared S_5–Fe_3O_4-300, S_5–Fe_3O_4-300, and S_5–Fe_3O_4-300 exhibited similar change trends in the presence of competing cations. The presence of Mg^{2+} with 0.50 mM slightly impeded the adsorption capacity of S_5–Fe_3O_4-300, S_5–Fe_3O_4-300, and S_5–Fe_3O_4-300 by 7.71%, 5.18%, and 18.21%, respectively. In addition, the inhibitory effect of Cd^{2+}, Cu^{2+}, and Zn^{2+} on the adsorption performance of S_x–Fe_3O_4 was slightly more pronounced than under the presence of Mg^{2+}, Ca^{2+}, since they may compete at the active sites through the favorable affinity interaction, thus hindering the Pb(II) removal. When the concentration of competing ions was raised, its impact became more noticeable, and S_x–Fe_3O_4 exhibited a similar trend. Overall, the removal capacity of Pb(II) with S_5–Fe_3O_4-300 can maintain over 80% of its original performance with the coexistence of competing cations at 0.50 mM. Overall, S_x–Fe_3O_4 can selectively remove Pb(II) from water, arising from the sulfur doping that provides active sites to Pb(II) through soft–soft interactions, which also demonstrated the potential of S_x–Fe_3O_4 as an effective adsorbent for Pb(II) adsorption.

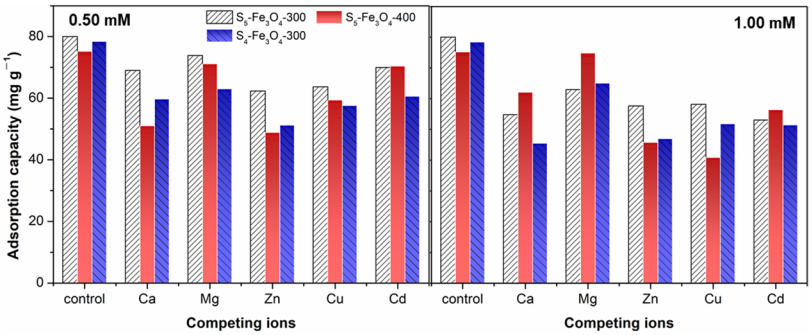

Figure 6. The effect of competing ions on the adsorption of Pb(II) with S_x–Fe_3O_4.

4. Conclusions

In this study, sulfur-doped Fe_3O_4 was fabricated through a calcination approach, which demonstrated favorable characteristics, magnetic separation, and effective Pb(II) adsorption performance. The XRD, TEM, FTIR, and VSM analyses demonstrated the successful synthesizing of S_x–Fe_3O_4 with sufficient magnetic separation properties. We also investigated the effects of the calcination temperature and content of sulfur doping on the characteristics and adsorption capability of S_x–Fe_3O_4. The crystalline structure was a benefit to the facile separation and introduction of sulfur, leading to the enhanced adsorption of Pb(II). Within the investigated range, there was a linear correlation between the adsorption capacity and the sulfur content in S_x–Fe_3O_4, with a high correlation of $R^2 = 0.989$. The performance of S_x–Fe_3O_4 enhanced with the increase of the sulfur content. The sulfur doping increased Pb(II) adsorption capacity, with a maximum capacity synthesized at 300 °C and a S–Fe molar ratio of 5 that was 4.18 times higher than Fe_3O_4. S_x–Fe_3O_4 exhibited selective adsorption with the coexisting of Mg^{2+} and Ca^{2+}, while inhibition was observed in the presence of Cu^{2+} and Cd^{2+}, which hold strong affinities to sulfur active sites. The adsorption enhancement of S_x–Fe_3O_4 mostly resulted from the doped sulfur that provided active sites for Pb(II) through soft–soft interaction between the soft base of sulfur and soft acid of Pb(II) and surface adsorption. The high Pb(II) adsorption performance and magnetic properties indicated that the sulfur-doped magnetic iron oxides could be a promising adsorbent candidate for Pb(II) removal from water.

Supplementary Materials: The following supporting information can be downloaded: https://www.mdpi.com/article/10.3390/w15203667/s1, Figure S1: Test of pseudo-first-order model for adsorption of Pb (II) on different adsorbents. The symbols are experimental data and the solid lines represent the fitted curves; Table S1: Adsorption kinetics parameters for pseudo-first-order and pseudo-second-order model of Pb (II) adsorption.; Table S2: Weight Percentage of major elements of S-Fe_3O_4 synthesized with different S/Fe molar ratio from XRF analysis.

Author Contributions: Conceptualization, L.K. and L.L.; methodology, J.X. and X.H.; validation, X.H.; formal analysis, C.Z. and M.P.; investigation, J.X. and X.H.; data curation, X.H.; writing—original draft preparation, J.X. and M.P.; writing—review and editing, L.K., T.H. and R.I.; visualization, J.X., M.P., L.K. and X.H.; supervision, L.K. and L.L.; project administration, L.K. and L.L.; funding acquisition, L.K. and L.L. All authors have read and agreed to the published version of the manuscript.

Funding: This research was supported by the National Natural Science Foundation of China (NSFC 42007125, 22175113); Joint Funds of the National Natural Science Foundation of China (No. U21A20320); China Postdoctoral Science Foundation (2021M702115).

Data Availability Statement: The data presented in this study are available on request from the corresponding author.

Conflicts of Interest: The authors declare no conflict of interest.

References

1. Peng, Q.; Guo, J.; Zhang, Q.; Xiang, J.; Liu, B.; Zhou, A.; Liu, R.; Tian, Y. Unique Lead Adsorption Behavior of Activated Hydroxyl Group in Two-Dimensional Titanium Carbide. *J. Am. Chem. Soc.* **2014**, *136*, 4113–4116. [CrossRef] [PubMed]
2. Zhang, Q.; Du, Q.; Hua, M.; Jiao, T.; Gao, F.; Pan, B. Sorption Enhancement of Lead Ions from Water by Surface Charged Polystyrene-Supported Nano-Zirconium Oxide Composites. *Environ. Sci. Technol.* **2013**, *47*, 6536–6544. [CrossRef] [PubMed]
3. Tang, J.; Zhao, B.; Lyu, H.; Li, D. Development of a novel pyrite/biochar composite (BM-FeS2@BC) by ball milling for aqueous Cr(VI) removal and its mechanisms. *J. Hazard. Mater.* **2021**, *413*, 125415. [CrossRef] [PubMed]
4. Zhou, Q.; Yang, N.; Li, Y.; Ren, B.; Ding, X.; Bian, H.; Yao, X. Total concentrations and sources of heavy metal pollution in global river and lake water bodies from 1972 to 2017. *Glob. Ecol. Conserv.* **2020**, *22*, e00925. [CrossRef]
5. Ding, J.; Pu, L.; Wang, Y.; Wu, B.; Yu, A.; Zhang, X.; Pan, B.; Zhang, Q.; Gao, G. Adsorption and Reduction of Cr(VI) Together with Cr(III) Sequestration by Polyaniline Confined in Pores of Polystyrene Beads. *Environ. Sci. Technol.* **2018**, *52*, 12602–12611. [CrossRef] [PubMed]
6. Ma, L.; Wang, Q.; Islam, S.M.; Liu, Y.; Ma, S.; Kanatzidis, M.G. Highly Selective and Efficient Removal of Heavy Metals by Layered Double Hydroxide Intercalated with the MoS42- Ion. *J. Am. Chem. Soc.* **2016**, *138*, 2858–2866. [CrossRef]
7. Othman, Z.; Mackey, H.R.; Mahmoud, K.A. A critical overview of MXenes adsorption behavior toward heavy metals. *Chemosphere* **2022**, *295*, 133849. [CrossRef]
8. Liu, Y.; Ke, Y.; Shang, Q.; Yang, X.; Wang, D.; Liao, G. Fabrication of multifunctional biomass-based aerogel with 3D hierarchical porous structure from waste reed for the synergetic adsorption of dyes and heavy metal ions. *Chem. Eng. J.* **2023**, *451*, 138934. [CrossRef]
9. Ji, C.; Xu, M.; Yu, H.; Lv, L.; Zhang, W. Mechanistic insight into selective adsorption and easy regeneration of carboxyl-functionalized MOFs towards heavy metals. *J. Hazard. Mater.* **2022**, *424*, 127684. [CrossRef]
10. Fu, K.; Liu, X.; Yu, D.; Luo, J.; Wang, Z.; Crittenden, J.C. Highly Efficient and Selective Hg(II) Removal from Water Using Multilayered Ti(3)C(2)O(x) MXene via Adsorption Coupled with Catalytic Reduction Mechanism. *Environ. Sci. Technol.* **2020**, *54*, 16212–16220. [CrossRef]
11. Haounati, R.; Ighnih, H.; Ouachtak, H.; Malekshah, R.E.; Hafid, N.; Jada, A.; Addi, A.A. Z-Scheme g-C3N4/Fe_3O_4/Ag3PO4@Sep magnetic nanocomposites as heterojunction photocatalysts for green malachite degradation and dynamic molecular studies. *Colloids Surf. A Physicochem. Eng. Asp.* **2023**, *671*, 131509. [CrossRef]
12. Ighnih, H.; Haounati, R.; Ouachtak, H.; Regti, A.; El Ibrahimi, B.; Hafid, N.; Jada, A.; Taha, M.L.; Addi, A.A. Efficient removal of hazardous dye from aqueous solutions using magnetic kaolinite nanocomposite: Experimental and Monte Carlo simulation studies. *Inorg. Chem. Commun.* **2023**, *153*, 110886. [CrossRef]
13. Leonel, A.G.; Mansur, A.A.; Mansur, H.S. Advanced Functional Nanostructures based on Magnetic Iron Oxide Nanomaterials for Water Remediation: A Review. *Water Res.* **2021**, *190*, 116693. [CrossRef]
14. Yantasee, W.; Warner, C.L.; Sangvanich, T.; Addleman, R.S.; Carter, T.G.; Wiacek, R.J.; Fryxell, G.E.; Timchalk, C.; Warner, M.G. Removal of Heavy Metals from Aqueous Systems with Thiol Functionalized Superparamagnetic Nanoparticles. *Environ. Sci. Technol.* **2007**, *41*, 5114–5119. [CrossRef]
15. Zhang, S.; Zhang, Y.; Liu, J.; Xu, Q.; Xiao, H.; Wang, X.; Xu, H.; Zhou, J. Thiol modified Fe_3O_4@SiO2 as a robust, high effective, and recycling magnetic sorbent for mercury removal. *Chem. Eng. J.* **2013**, *226*, 30–38. [CrossRef]
16. Zhang, X.; Qian, J.; Pan, B. Fabrication of Novel Magnetic Nanoparticles of Multifunctionality for Water Decontamination. *Environ. Sci. Technol.* **2016**, *50*, 881–889. [CrossRef]
17. Luan, X.; Zhu, D.; He, P.; Han, P.; Wei, G. Self-assembled peptide nanosheets functionalized with Fe_3O_4 nanoparticles with enhanced nanozymatic activity for sensitive colorimetric detection and selective adsorption of Hg^{2+}. *Environ. Sci. Nano* **2023**. [CrossRef]
18. Wang, T.; Zhang, L.; Li, C.; Yang, W.; Song, T.; Tang, C.; Meng, Y.; Dai, S.; Wang, H.; Chai, L.; et al. Synthesis of Core-Shell Magnetic Fe_3O_4@poly(m-Phenylenediamine) Particles for Chromium Reduction and Adsorption. *Environ. Sci. Technol.* **2015**, *49*, 5654–5662. [CrossRef]
19. Tang, N.; Niu, C.-G.; Li, X.-T.; Liang, C.; Guo, H.; Lin, L.-S.; Zheng, C.-W.; Zeng, G.-M. Efficient removal of Cd^{2+} and Pb^{2+} from aqueous solution with amino- and thiol-functionalized activated carbon: Isotherm and kinetics modeling. *Sci. Total. Environ.* **2018**, *635*, 1331–1344. [CrossRef]
20. Kromah, V.; Zhang, G. Aqueous Adsorption of Heavy Metals on Metal Sulfide Nanomaterials: Synthesis and Application. *Water* **2021**, *13*, 1843. [CrossRef]
21. Chen, Y.; Liang, W.; Li, Y.; Wu, Y.; Chen, Y.; Xiao, W.; Zhao, L.; Zhang, J.; Li, H. Modification, application and reaction mechanisms of nano-sized iron sulfide particles for pollutant removal from soil and water: A review. *Chem. Eng. J.* **2019**, *362*, 144–159. [CrossRef]
22. Gong, Y.; Liu, Y.; Xiong, Z.; Zhao, D. Immobilization of Mercury by Carboxymethyl Cellulose Stabilized Iron Sulfide Nanoparticles: Reaction Mechanisms and Effects of Stabilizer and Water Chemistry. *Environ. Sci. Technol.* **2014**, *48*, 3986–3994. [CrossRef] [PubMed]
23. Li, K.; Hanpei, Y.; Lina, W.; Siqi, C.; Ruichen, Z.; Junming, W.; Xiaona, L. Facile integration of FeS and titanate nanotubes for efficient removal of total Cr from aqueous solution: Synergy in simultaneous reduction of Cr(VI) and adsorption of Cr(III). *J. Hazard Mater.* **2020**, *398*, 122834. [CrossRef] [PubMed]

24. Wu, J.; Wang, X.-B.; Zeng, R.J. Reactivity enhancement of iron sulfide nanoparticles stabilized by sodium alginate: Taking Cr (VI) removal as an example. *J. Hazard. Mater.* **2017**, *333*, 275–284. [CrossRef]
25. Cui, H.-J.; Shi, J.-W.; Yuan, B.; Fu, M.-L. Synthesis of porous magnetic ferrite nanowires containing Mn and their application in water treatment. *J. Mater. Chem. A* **2013**, *1*, 5902–5907. [CrossRef]
26. Xue, S.; Fan, J.; Wan, K.; Wang, G.; Xiao, Y.; Bo, W.; Gao, M.; Miao, Z. Calcium-Modified Fe_3O_4 Nanoparticles Encapsulated in Humic Acid for the Efficient Removal of Heavy Metals from Wastewater. *Langmuir* **2021**, *37*, 10994–11007. [CrossRef]
27. Qi, Z.; Joshi, T.P.; Liu, R.; Liu, H.; Qu, J. Synthesis of Ce(III)-doped Fe_3O_4 magnetic particles for efficient removal of antimony from aqueous solution. *J. Hazard. Mater.* **2017**, *329*, 193–204. [CrossRef] [PubMed]
28. Patil, A.B.; Patil, K.R.; Pardeshi, S.K. Ecofriendly synthesis and solar photocatalytic activity of S-doped ZnO. *J. Hazard. Mater.* **2010**, *183*, 315–323. [CrossRef]
29. Yang, K.; Peng, H.; Wen, Y.; Li, N. Re-examination of characteristic FTIR spectrum of secondary layer in bilayer oleic acid-coated Fe_3O_4 nanoparticles. *Appl. Surf. Sci.* **2010**, *256*, 3093–3097. [CrossRef]
30. Huberty, J.; Madix, R. An FTIR study of the bonding of methoxy on Ni(100): Effects of coadsorbed sulfur, carbon monoxide and hydrogen. *Surf. Sci.* **1996**, *360*, 144–156. [CrossRef]
31. Huang, F.; Rad, A.T.; Zheng, W.; Nieh, M.P.; Cornelius, C.J. Hybrid organic-inorganic 6FDA-6pFDA and multi-block 6FDA-DABA polyimide SiO_2-TiO_2 nanocomposites: Synthesis, FFV, FTIR, swelling, stability, and X-ray scattering. *Polymer* **2017**, *108*, 105–120. [CrossRef]
32. Wei, Y.; Han, B.; Hu, X.; Lin, Y.; Wang, X.; Deng, X. Synthesis of Fe_3O_4 Nanoparticles and Their Magnetic Properties. In Proceedings of the 2011 Chinese Materials Conference, Beijing, China, 18–23 August 2011; Volume 27, pp. 632–637.
33. Jegadeesan, G.; Al-Abed, S.R.; Sundaram, V.; Choi, H.; Scheckel, K.G.; Dionysiou, D.D. Arsenic sorption on TiO2 nanoparticles: Size and crystallinity effects. *Water Res.* **2010**, *44*, 965–973. [CrossRef] [PubMed]
34. Dixit, S.; Hering, J.G. Comparison of Arsenic(V) and Arsenic(III) Sorption onto Iron Oxide Minerals: Implications for Arsenic Mobility. *Environ. Sci. Technol.* **2003**, *37*, 4182–4189. [CrossRef] [PubMed]
35. Hu, W.; Yang, L.; Shao, P.; Shi, H.; Chang, Z.; Fang, D.; Wei, Y.; Feng, Y.; Huang, Y.; Yu, K.; et al. Proton Self-Enhanced Hy-droxyl-Enriched Cerium Oxide for Effective Arsenic Extraction from Strongly Acidic Wastewater. *Environ. Sci. Technol.* **2022**, *56*, 10412–10422. [CrossRef]
36. Tseng, R.-L.; Wu, F.-C. Inferring the favorable adsorption level and the concurrent multi-stage process with the Freundlich constant. *J. Hazard. Mater.* **2008**, *155*, 277–287. [CrossRef]